# Lawrence Berkeley National Laboratory
**Recent Work**

**Title**
Fluorination-Enhanced Surface Stability of Cation-Disordered Rocksalt Cathodes for Li-Ion Batteries

**Permalink**

**Journal**

**ISSN**

**Authors**
Li, L
Lun, Z
Chen, D
et al.

**Publication Date**

**DOI**

Peer reviewed

# Fluorination-Enhanced Surface Stability of Cation-Disordered Rocksalt Cathodes for Li-Ion Batteries

*Linze Li,[1†] Zhengyan Lun,[2†] Dongchang Chen,[3] Yuan Yue,[3] Wei Tong,[3] Guoying Chen,[3] Gerbrand Ceder,[2*] Chongmin Wang[1*]*

1. Environmental Molecular Sciences Laboratory, Pacific Northwest National Laboratory, 902 Battelle Boulevard, Richland, WA 99354, USA
2. Department of Materials Science and Engineering, University of California – Berkeley, 328 Hearst Mining Memorial Building, Berkeley, CA 94720, USA
3. Energy Storage and Distributed Resources Division, Lawrence Berkeley National Laboratory, Berkeley, CA 94720 USA

[†] These authors contributed equally
[*] To whom correspondence may be addressed.
Email: gceder@berkeley.edu, chongmin.wang@pnnl.gov

**ABSTRACT**

**Cation-disordered rocksalt (DRX) materials have emerged as a class of novel high-capacity cathodes for Li-ion batteries. However, commercialization of DRX cathodes will require reducing their capacity decay, which has been associated with oxygen loss during cycling. Recent studies have shown that fluorination of DRX cathodes can effectively reduce the oxygen loss and improve the cycling stability; however, the underlying atomic-scale mechanisms remain elusive. Herein, using a combination of electrochemical measurements, scanning transmission electron microscopy, and electron energy loss spectroscopy, we examine the correlation between the electrochemical properties and structural evolution in Mn-redox-based DRX cathodes, $Li_{1.2}Ti_{0.4-x}Mn_{0.4+x}O_{2.0-x}F_x$ (x = 0 and 0.2). We find that fluorination strongly suppresses structural amorphization and void formation initiated from the particle surface, therefore greatly enhancing the cyclability of the cathode. We further reveal a novel rocksalt-to-spinel-like structural transformation in the DRX bulk, which surprisingly contributes to a gradual capacity increase during cycling. Our results provide important insight for the design of novel DRX cathodes with high capacity and long cycle life.**

## Introduction

With the tremendous growth of Li-ion-based energy storage for portable electronics, electric vehicles, and grid storage, the need for the development of novel cathode materials with enhanced electrochemical performance, reduced cost, and less reliance on cobalt and/or nickel, continues to increase.[1] Layered $LiNi_xMn_yCo_zO_2$ (x + y + z = 1) with the $\alpha$-$NaFeO_2$ structure ($R$-$3m$ space group), typically referred to as NMC, are currently the most widely applied cathode materials for Li-ion batteries because of their large capacity and good stability.[2-4] The ordered arrangement of Li and transition metals (TMs) in layered NMC provides clear paths for Li-ion transport within the 2D Li slabs. The irreversible cation migration, which creates cation disorder, is detrimental to Li-ion transport in the layered lattice because it blocks Li migration channels.[5-9] The key reason for using Ni, Mn, and Co in the layered structure is that they are among the very few TMs that do not significantly migrate to Li layers upon electrochemical cycling in either their pristine oxidation states or oxidized states.[10-13] However, with the Li-ion industry growing to 1 TWh per year, more than a million tons of Co and Ni combined will be needed for producing well-ordered layered structures, which create severe resource constraints and thus require a move-away to a larger chemical space involving more earth-abundant elements.[11, 14]

Recent progress in the development of Li-excess disordered rocksalt (DRX) cathodes has revealed that facile Li transport can also occur even with cation disorder.[15, 16] Such Li transport is enabled by the formation of a Li-rich percolating network in the DRX lattice.[15] This discovery has lifted the restriction that Li-ion cathodes must be layered and remain layered upon cycling to achieve high capacity, thereby opening up a much broader chemical space for cathode synthesis.[10, 17] The use of various TMs, in some cases only earth-abundant ones (*e.g.*, Fe, Mn, and Ti), has generated a large number of Li-excess DRX oxide cathodes, including $Li_{1.211}Mo_{0.467}Cr_{0.3}O_2$,[15] $Li_4Mn_2O_5$,[18] $Li_{1.2}Mn_{0.4}Ti_{0.4}O_2$,[19] $Li_{1.2}Ni_{0.333}Ti_{0.333}Mo_{0.133}O_2$,[20] $Li_{1.2}Mn_{0.6}Nb_{0.2}O_2$,[21] $Li_{1.25}Nb_{0.25}Mn_{0.5}O_2$,[22] $Li_{1.2}Ni_{1/3}Ti_{1/3}W_{2/15}O_2$,[23] $LiFe_{0.5}V_{0.5}O_2$,[24] $Li_{1.25}Nb_{0.25}V_{0.5}O_2$,[25] and $Li_{1.2}Mn_{0.2}V_{0.6}O_2$.[26] One drawback of these DRX oxide cathodes, however, is that the Li-excess composition constrains the amount of redox-active TM and thus usually requires high levels of O redox, which can trigger significant O loss and rapid capacity decay during cycling.[20, 27, 28] To overcome this drawback, the strategy of using F substitution for O in DRX has been explored.[20, 21, 26, 29, 30] Unlike in conventional layered cathodes, where O-to-F substitution is not feasible, substantial levels of F doping can be achieved in DRX materials because of the presence of local TM-poor, Li-rich environments that are highly favorable for fluorination.[29, 31] Increasing the F content enables the incorporation of a larger TM-redox reservoir in DRX materials without sacrificing Li content, and this approach has been demonstrated as an effective route for reducing irreversible O loss and improving the cyclability of various DRX cathodes, such as $Li_{1.2}Ni_{1/3}Ti_{1/3}Mo_{2/15}O_2$ and $Li_{1.2}Nb_{0.2}Mn_{0.6}O_2$.[20, 21] With heavily fluorination, it is also possible to incorporate multi-electron TM redox, such as $V^{3+}/V^{5+}$ redox in $Li_2VO_2F$,[32] $Mn^{2+}/Mn^{4+}$ redox in $Li_2Mn_{2/3}Nb_{1/3}O_2F$,[30] and $Mo^{3+}/Mo^{6+}$ redox in $Li_2MoO_2F$.[33] Remarkably, as a result of

such multi-electron TM redox, negligible oxygen release is observed even when charging up to 5.0V with a high capacity of > 300 mAh g$^{-1}$ in the heavily fluorinated $Li_2Mn_{2/3}Nb_{1/3}O_2F$.[30]

However, despite the experimental and theoretical studies conducted on DRX cathodes thus far, a detailed microscopic understanding of the capacity decay in DRX oxides remains lacking. Herein, using atomic-resolution scanning transmission electron microscopy (STEM) coupled with electron energy loss spectroscopy (EELS), we examine the structural evolution and chemical reconstruction induced by electrochemical cycling in a model DRX oxide cathode, $Li_{1.2}Ti_{0.4}Mn_{0.4}O_{2.0}$ (LTMO), and its fluorinated variant, $Li_{1.2}Ti_{0.2}Mn_{0.6}O_{1.8}F_{0.2}$ (LTMOF). We reveal a high level of structural degradation initiated from the particle surface, including amorphization and void formation, in cycled LTMO particles, which impede Li transport through the surface and may be closely correlated to the capacity fade. This surface degradation is much less prominent in cycled LTMOF particles, indicating the crucial role of fluorination in enhancing the structural stability of DRX cathodes, thereby greatly improving the cycling stability of the cathode. Furthermore, we observe a disordered-to-spinel-like structural transformation in the DRX bulk. While in previous studies an irreversible structural change in a cathode material would usually lead to capacity degradation, here we find that this transformation surprisingly results in a capacity increase in LTMOF upon cycling.

## Results

### Bulk properties and electrochemical performance

LTMO and LTMOF cathode particles were synthesized using a one-step solid-state synthesis method.[21] The as-synthesized particles were further processed using a ball-milling procedure with carbon black during the electrode fabrication, and the rotation speed was purposely set to a moderate value of 250 rpm (Retsch PM200) to preserve the crystallinity of the particles for transmission electron microscopy (TEM) analysis. X-ray diffraction (XRD) patterns and the corresponding Rietveld refinements of the LTMO and LTMOF particles are presented in Fig. S1 and Table S1, respectively, confirming the cubic rocksalt structure with *Fm-3m* symmetry with no observable impurity peaks. The lattice constant of LTMOF (4.1540 Å) is slightly larger than that of LTMO (4.1458 Å). As observed in the scanning electron microscopy (SEM) images (Fig. S2a, b) and TEM images (Fig. 1a,c), the as-synthesized LTMO and LTMOF particles are mostly 1–5 μm in diameter, with smaller sub-micron particles also observed. After the ball-milling procedure, the particle sizes of both LTMO and LTMOF are reduced to 0.2–1.0 μm (Fig. S2c, d). The STEM images and corresponding energy-dispersive X-ray spectroscopy (EDS) elemental maps in Fig. 1b and d, respectively, show that the cations and anions are uniformly distributed at the particle level in both samples.

To measure the electrochemical properties, cathodes made with LTMO and LTMOF were cycled between 1.5 and 4.8 V vs. Li/Li$^+$ at a specific current of 20 mA/g for 50 cycles. Fig. 1e and f

present the charge and discharge voltage profiles for the 1st, 10th, 25th and 50th cycles and capacity retention curves for the LTMO and LTMOF cathodes, respectively. We note that the capacity fluctuation near the 18th cycle in both materials was caused by unintended temperature fluctuation. The LTMO cathodes delivered an initial discharge capacity of 191 mAh g$^{-1}$, and the capacity decayed to 145 mAh g$^{-1}$ after 50 cycles. In contrast, the LTMOF cathode exhibited a lower discharge capacity (151 mAh g$^{-1}$) in the 1st cycle; however, unexpectedly, the reversible capacity continued to increase as cycling progressed, reaching 227 mAh g$^{-1}$ after 50 cycles. Although fluorination of DRX cathodes is known to lead to improved capacity retention,[20, 21] our results here further reveal the interesting phenomenon of increasing capacity during cycling in the LTMOF cathode.

**Atomic-scale structural reconstruction and chemical redistribution initiated from the surface**

The morphology of the LTMO and LTMOF cathode particles shown in TEM images (Fig. S3) did not change after 50 cycles, and the distribution of cations and anions revealed by EDS elemental maps (Fig. S4) of both cycled cathode particles remained uniform at the particle level. To examine the evolution of the atomic-scale structure under electrochemical cycling in both LTMO and LTMOF particles, STEM high-angle annular dark-field (HAADF) imaging was performed. Nanoscale regions near the surfaces of the LTMO particles in the pristine state and discharged state after 50 cycles are shown in Fig. 2a and b, respectively. In the pristine state, the rocksalt crystalline structure is uniform from the inner bulk to the outer surface. In contrast, after 50 cycles, crystallinity was only preserved in the inner bulk, whereas the ~10-nm-thick surface region has become mostly amorphous and populated with nanosized voids (evident as the darker nanoregions in the lattice in Fig. 2b). These voids are nanoscale regions featured by loss of elements in the local lattice, as reduced intensities of both O and TMs inside the voids was confirmed by comparing the EELS elemental maps of the pristine (Fig. S5) and cycled (Fig. S6) LTMO particles.

To explore any chemical redistribution or changes of the oxidation states associated with the structural evolution in LTMO, EELS spectra of the O $K$-edges and Ti and Mn $L$-edges were collected at 7 different locations near the surfaces of the pristine (Fig. S7) and cycled (Fig. S8) LTMO particles. The extracted atomic-percentage profiles of Ti, Mn, and O for the pristine and cycled LTMO particles are plotted in Fig. 2c and d, respectively. Note that because only these 3 elements were quantified, the sum of the 3 values (atomic percentages of Ti, Mn, and O) equals 100% at each point in Fig. 2c and d. The measured atomic-percentage values in the bulk of pristine and cycled LTMO particles are both close to the values calculated from the stoichiometric chemical formula of LTMO (Table S2). The results in Fig. 2c and d indicate that although the Ti distribution is mostly uniform from the bulk to the surface in both the pristine and cycled LTMO, there is much more of a gradient in the Mn and O distributions, resulting in

O-deficient (and Mn-rich) surface layers in both materials. The O-deficient layer on the pristine LTMO sample could be due to surface O loss during the cathode synthesis. The thickness of the O-deficient layer grew from ~5 nm in the pristine material to approximately 14 nm after 50 cycles, which is believed to be caused by irreversible oxygen release, as observed in many DRX oxides.[20, 21] Correspondingly, the reduction of Ti and Mn valences, as evidenced by the suppression of the Ti $L_2$ and $L_3$ pre-peak intensities, the shift of the Mn $L_3$ peak to lower energies, and the increase of the Mn $L_3/L_2$ ratios,[34, 35] was restricted to the very surface layer (~5-nm thick) in the pristine sample but extended into a much deeper region below the surface (~14-nm thick) after 50 cycles (Fig. S7 and S8).

A similar analysis was also performed on LTMOF. Atomic-scale STEM HAADF images of nanoscale regions near the surfaces of LTMOF particles in the pristine state and discharged state after 50 cycles are presented in Fig. 2e and f, respectively. Unlike for LTMO, which exhibited cycling-induced surface degradation, the crystalline structure of LTMOF is maintained from the bulk to surface after cycling. The corresponding EELS elemental maps and EELS spectra collected at 5 different locations below the surfaces of both the pristine and cycled LTMOF are presented in Fig. S9–13. Note that due to the low concentration of F in LTMOF, the F $K$-edges cannot be detected by EELS in our work. The extracted atomic-percentage profiles of Ti, Mn, and O for the pristine and cycled LTMOF particles are presented in Fig. 2g and h, respectively. The measured atomic-percentage values in the bulk of pristine and cycled LTMOF particles are both close to the values calculated from the stoichiometric chemical formula of LTMOF (Table S3). In Fig. 2g and h, O-deficient (and Ti-rich) non-uniform distributions were observed below the surface of LTMOF, though over a reduced thickness compared to LTMO, with O-deficient layers of ~4 and ~8 nm before and after 50 cycles, respectively. A corresponding reduction of the Ti and Mn valences, as evidenced by the suppression of the Ti $L_2$ and $L_3$ pre-peak intensities, the shift of the Mn $L_3$ peak to lower energies, and the increase of the Mn $L_3/L_2$ ratios,[34, 35] was also observed within the O-deficient surface layers in LTMOF but with a reduced penetration depth compared to LTMO (Fig. S12 and S13). Further, STEM EDS linescan measurements were performed (Fig. S14), confirming that the non-uniform elemental distribution is restricted to the surface areas of both LTMO and LTMOF, while the compositions in the bulk of the cycled cathode particles remain mostly unperturbed. With EDS, the F concentration is also measured, giving a value of ~ 3 at% in the bulk (Fig. S14), while the designated amount of F in the stoichiometric formula of LTMOF is ~ 7 at% (note that because only Ti, Mn, O, and F were quantified by EDS, the sum of the atomic percentages of Ti, Mn, O, and F equals 100 at%).

**Rocksalt-to-spinel-like structural transformation**

Upon cycling a transformation from the rocksalt to a spinel-like structure was observed in both the LTMO and LTMOF particles. Electron diffraction patterns of LTMO before and after cycling are presented in Fig. 3a and b, respectively. For pristine LTMO, the phase-pure DRX structure is

evidenced by the sharp spots corresponding to long-range DRX ordering, with the circle-like diffused intensity patterns originating from the short-range cation order (SRO).[17, 36] For LTMO after 50 cycles, additional diffraction spots (marked by white arrows in Fig. 3b) appeared at the centers of the circle-like diffused intensity patterns, indicating the formation of spinel-like structures.[37] A similar change in structural information was also observed in the fast Fourier transforms of the STEM HAADF images of nanoscale regions in the bulk of the pristine and cycled LTMO (Fig. 3c,d). The STEM HAADF image of cycled LTMO was further processed by filtering the structural information in the Fourier transform. In the image filtering process, masks that only allow structural information from either the rocksalt cubic lattice or the spinel-like lattice were applied (Fig. 3e), and then inverse Fourier transform were performed to get filtered images that only contain either the rocksalt (purple) or spinel-like (green) structures (Fig. 3f, g). Finally, a combination of the two filtered images resulted in a single image (Fig. 3h) showing that the nanosized spinel-like domains (green) are dispersed in the rocksalt matrix (purple).

Similar changes in the electron diffraction patterns indicating this rocksalt-to-spinel-like structural transformation were also observed for the LTMOF particles (Fig. S15). Further details on this structural evolution were obtained using atomic-scale STEM HAADF imaging and analysis of LTMOF particles at different stages of the cycling process (Fig, 4). In both the pristine LTMOF (Fig. 4a) and the discharged LTMOF after the 1st cycle (Fig. 4b), phase-pure DRX structures were observed. In the discharged LTMOF after 20 cycles (Fig. 4c) and 50 cycles (Fig. 4d), spinel-like structures were formed. The spinel-like areas in the sample after 50 cycles were generally larger than those after 20 cycles. These observations suggest that the structural change occurs gradually and continuously upon cycling. To further illustrate the mixed-phase structure after the transformation, a magnified STEM HAADF image of a boundary between a rocksalt and spinel-like region in LTMOF after 50 cycles and the corresponding filtered image are presented in Fig. 4e and f, respectively. In these images, the strong intensities observed at the tetrahedral ($T_d$) 8a sites in the spinel-like structure suggest that these sites are not purely occupied by Li atoms but also by TM atoms. This is because the intensity of a HAADF STEM image is directly proportional to the atomic number $Z$ as $Z^{1.7}$; thus, such imaging can only be used for resolving the heavy TM atomic columns and not for the light Li columns.[38] The occupancy of TMs at the $T_d$-8a sites indicates a disordered spinel-like structure, which is different from the conventional spinel phase, where the $T_d$-8a and $O_h$-16d sites are occupied by Li and TM, respectively. EELS elemental maps of the mixed-phase structures in LTMOF after 20 cycles indicate that there was no elemental segregation within different phases (rocksalt or spinel-like) (Fig. S11). In addition, EELS spectra of the Ti and Mn $L$-edges confirmed that the TM valences were consistent across different phases at the same depth beneath the surface, as evidenced by their similar Ti $L_2$ and $L_3$ pre-peak intensities and Mn $L_3$ peak positions (Fig. S11). Additional XRD measurements of LTMOF electrode films before and after cycling have also been carried out, as shown in Fig. S16. In the XRD pattern, although the signal from the binder

(PTFE) and the characteristic peak from spinel-like ordering highly overlap at ~18°, we can still see a slight shift of the peak position at ~18° in the cycled LTMOF, which could indicate the formation of spinel-like ordering.

The formation of spinel-like structures upon cycling also leads to changes in the shape of voltage profiles in LTMOF, as shown in Fig. 1e and 1f. It can be observed that the capacity increment mainly comes from the emerging plateau-like feature around 4V and the elongated and flattened plateau-like feature around 3V. These two additional plateau-like features match the characteristics of typical spinel cathodes, but the lengths of the plateaus do not exactly match that in the perfect spinel structure.[39] This indicates that the cycling-induced spinel-like structure in LTMOF is partially disordered (rather than a perfect spinel structure), which is consistent to our microscopic observation (Fig. 4). In fact, similar electrochemical signatures suggesting the formation of spinel-like structures have also been observed during the cycling of $Li_{1.2}Mn_{0.625}Nb_{0.175}O_{1.95}F_{0.05}$ cathodes,[40, 41] indicating that the rocksalt to spinel-like structural transformation may be a common phenomenon existing in Mn-based DRX cathodes.

## Discussion

The structural evolutions in LTMO and LTMOF upon cycling are schematically summarized in Fig. 5a and b, respectively. The most dramatic difference between these two materials was the strong near-surface degradation in LTMO, which is correlated to the significant O loss.[20, 21, 42] In fact, our EELS measurements indicate that the thickness of the O-deficient surface layer in LTMO (~14 nm) (Fig. 2d) after 50 cycles was much larger than that in LTMOF (~8 nm) (Fig. 2h), confirming that much more severe O loss occurred in LTMO. Strong O loss from Li-excess materials is usually triggered by excess usage of O redox. It has been known that in DRX materials, the redox potential of $Ti^{3+}/Ti^{4+}$ sits below 1.5V,[30] so $Ti^{4+}$ remain redox in-active within our cycling voltage window and does not participate in the charge compensation. In the LTMO, the $Mn^{3+/4+}$ redox can only contribute 131 mAh $g^{-1}$, leaving the rest (approximately one third of the capacity) compensated by O redox, which is less stable than TM redox and leads to oxygen loss. The deteriorated surface layer left behind after O loss in LTMO mostly becomes amorphous, with nanosized voids formed inside (Fig. 5a), accompanied by a reduction of the oxidation states of the TMs (Fig. S7, S8) with potential TM densification (more TM and less Li compared with the stoichiometric composition). This TM-densified amorphous surface may no longer be Li-excess and blocks the migration pathway of Li ions through the surfaces in DRX cathodes, leading to the growth of surface impedance and capacity fading of LTMO, as observed in Fig. 1e. The formation of void near the surface region upon cycling is related to the kinetic factor of O loss, which is apparently initiated from particle surface. Since the surface is directly exposed to the electrolyte during the cycling, the structural degradation/amorphization should be

initiated from the surface. Actually, similar progressive inward growth of pore populated region from the surface of the particle has also been observed in the Li-rich layer structured cathode, where the excitation of anionic redox facilitates the migration of oxygen from the bulk lattice towards surface through surface oxygen vacancy mechanism.[43] It is believed that similar mechanism operates in the present case.

In contrast, fluorination leads to enhancement of the structural stability at the surface of LTMOF (Fig. 5b), as it can increase the redox-active TM content (that is, $Mn^{3+}$ in this study) without sacrificing Li, and thus reduce O redox and mitigate irreversible O loss during cycling. The Ti enrichment observed at the surface of LTMOF (Fig. 2g, h) could also be beneficial for reducing O loss during the cycling, because of the strong bonding between Ti and O.[44, 45] The reduced O loss and enhanced structural stability during the cycling of LTMOF is generally beneficial for maintaining the crystalline structure at the surface, which ensures facile Li transport through it.

A structural evolution from the rocksalt to a more spinel-like phase was also observed in our DRX cathodes and is presumably associated with the gradual capacity increase in LTMOF (Fig. 1f). Structural change when cycling ordered compounds that contain a lot of redox active Mn is well documented[46-49] and is assisted by the high mobility of $Mn^{3+}$ and $Mn^{2+}$.[50] We should point out that the "spinel-like" phase cannot be fully characterized and that it clearly has features of intermediates that have been previously identified in transformations between layered or orthorhombic $LiMnO_2$[50] and spinel $LiMn_2O_4$[51], including the presence of tetrahedral Mn. While the migration of Mn between octahedral and tetrahedral sites is known to be facile, creating Li-Mn dumbbells,[52] full rearrangement into a perfect spinel structures is much slower, and is likely to be hindered by the presence of the less mobile $Ti^{4+}$ ions. In addition, the presence of a $d^0$ element such as $Ti^{4+}$ will reduce the driving force to form spinel as it is known to stabilize the disordered rocksalt.[10]

Here, the phase-transformation-induced capacity growth appears to be a plausible mechanism, in contrast to the previous reports that irreversible phase transformation is usually detrimental for electrochemical properties.[53] According to previous studies, Li migration proceeds by Li hopping from one $O_h$ site to another $O_h$ site *via* an intermediate $T_d$ site (o–t–o diffusion) in the rocksalt-based lattice.[15] A $T_d$ site with no face-sharing TM, namely a 0-TM channel, provides the lowest energy barrier for Li migration.[15] The spinel structure has been shown to have improved Li-transport properties compared with layered and/or disordered rocksalt structures because of the well-connected "0-TM" Li-migration channels,[16] and partially disordered spinels have recently been shown to have extremely high rate capability.[54] Here, the capacity growth of LTMOF is consistent with the improved Li diffusion in the newly formed disordered spinel-like structures. And the DRX-to-disordered-spinel-like phase transformation occurring gradually and continuously in the bulk may explain why the capacity of LTMOF continuously increased upon cycling despite a certain degree of surface degradation (Fig. 1f, 2f,h). As for LTMO (Fig. 5a), the

occurrence of severe surface degradation and possibly smaller degree of bulk structural transformation (due to less $Mn^{3+}$) during cycling led to continuous capacity decay (Fig. 1e).

Finally, as a further demonstration of the beneficial effect of the formation of this spinel-like ordering, we compared the rate capability of the two materials before and after cycling (as shown in Fig. S17) by designing the following cycling protocol: the 1st to 5th cycles were measured at 10, 50, 100, 200, 500 mA g^{-1}, respectively; the 6th to 20th cycles were cycled at 20 mA g^{-1}; the 21st to 25th cycles were measured at 10, 50, 100, 200, 500 mA g^{-1}, respectively again. It can be observed that after 20 cycles, LTMOF demonstrates increased capacities at all different rates, indicating an improved rate capability (Li transport) induced by the formation of spinel-like cation ordering despite of slight surface degradation, while in comparison for LTMO, the capacities at various rates drop because of the severe surface degradation. This is consistent with our microscopic observations in Fig. 2 and Fig. 4.

## Conclusions

Using a combination of electrochemical measurements, scanning transmission electron microscopy, and electron energy loss spectroscopy, the correlation between the electrochemical properties and structural and chemical evolution induced by cycling in a DRX oxide cathode (LTMO) and a comparable DRX oxyfluoride cathode (LTMOF) were explored. The origin of capacity fading in LTMO was observed to be correlated to strong structural degradation, including amorphization and void formation initiated in the surface region. A beneficial effect of fluorination of the DRX cathode on improving the surface stability and thus the cyclability of DRX cathodes is revealed. Furthermore, local structure evolution from DRX to a disordered spinel-like structure was observed to occur gradually and continuously during cycling, within nanosized grains dispersed in the bulk of both LTMO and LTMOF. In conjunction with the well-preserved crystalline surface in LTMOF, the gradual structural transformation led to continuous growth of the capacity with increasing cycle number (<50 in this work). Our findings explain several important aspects of the atomic-scale mechanisms that underpin the electrochemical performance of DRX cathodes, providing fundamental insight for the development of next-generation cathode materials.

## Methods:

***Material synthesis and electrochemical test***: $Li_{1.2}Ti_{0.4}Mn_{0.4}O_{2.0}$ (LTMO) and $Li_{1.2}Ti_{0.2}Mn_{0.6}O_{1.8}F_{0.2}$ (LTMOF) cathodes were synthesized using a traditional solid-state method. $Li_2CO_3$ (Alfa Aesar, ACS, 99% min), $Mn_2O_3$ (Alfa Aesar, 99.9%), $TiO_2$ (Alfa Aesar, 99.9%), and LiF (Alfa Aesar, 99.99%) were used as precursors. All the precursors were stoichiometrically mixed in ethanol

(except for the addition of approximately 10% more $Li_2CO_3$ to compensate for possible loss during synthesis) using a Retsch PM 400 planetary ball mill at a rate of 180 rpm for 12 h. The precursors were then dried in a 70°C oven overnight and pelletized. The precursor pellets were sintered at 1000°C under argon atmosphere for 4 h. The pellets were then fast cooled at argon atmosphere, transferred to a glovebox, and ground into powders.

All the cathode films were composed of the active materials, Super C65 (Timcal), and polytetrafluoroethylene (PTFE, DuPont, Teflon 8A) at a weight ratio of 70:20:10. To make the cathode films, 350 mg of the as-synthesized active materials and 100 mg of Super C65 were mixed and ball-milled at 250 rpm for 6 h in an argon atmosphere using a Retsch PM200 planetary ball-mill, and PTFE was later added and manually mixed with the shaker-milled mixture for 40 min. The components were then rolled into thin films inside a glovebox. Commercial 1 M $LiPF_6$ in ethylene carbonate (EC) and dimethyl carbonate (DMC) solution (1:1 volume ratio) was used as the electrolyte. A glass microfiber filter (Whatman) was used as the separator. FMC Li metal foil was used as the anode. Coin cells were assembled inside the glovebox and tested on an Arbin battery test instrument at room temperature. The loading density of the films was approximately 3–4 mg cm$^{-2}$ based on the active materials.

***X-ray diffraction***: Lab XRD patterns were obtained using a Bruker D8 ADVANCE diffractometer (Cu source) in the 2θ range of 15°–85°. Rietveld refinement was performed using PANalytical X'pert HighScore Plus software.

***Transmission electron microscopy***: LTMO and LTMOF cathode particles for transmission electron microscopy (TEM) analysis were dispensed onto TEM lacey carbon grids inside an Ar-filled glovebox, without being exposed to any solutions during TEM sample preparation. TEM imaging and diffraction was performed on an aberration-corrected Titan 80-300™ scanning/transmission electron microscope (S/TEM) operated at 300 kV. The electron diffraction patterns were collected with a selected area diffraction (SAD) aperture of ~200 nm inserted. Scanning transmission electron microscopy (STEM) imaging, energy-dispersive X-ray spectroscopy (EDS) mapping, and Electron energy loss spectroscopy (EELS) microanalysis were performed on an aberration-corrected JEOL JEM-ARM200CF using an operation voltage of 200 kV. The convergence semi-angle was 20.6 mrad. Signals for semi-angles spanning from 68 to 280 mrad were collected for STEM HAADF imaging. The EDS data analysis was performed using the software "pathfinder", where the overlapped peaks were deconvolved using the stored standard reference spectra and a multiple linear least-squares fitting method. EELS data were collected with a post-column Gatan Image Filter (GIF) working at 0.25 eV/channel energy dispersion, with a EELS collection semi-angle of 42.9 mrad. The EELS spectra were processed by subtraction of the pre-edge power-law background using the Digital Micrograph software and subsequent removal of the post-edge background, which is fitted with a double arctangent step

function. The heights of the isolated $L_3$ and $L_2$ peaks were then used for calculating the $L_3/L_2$ ratios for Mn.

**Data Availability:**
All data that support the findings of this study have been included in the main text, supplementary information, and supplementary movies. Original data are kept at the Environmental Molecular Sciences Laboratory at Pacific Northwest National Laboratory and are available from the corresponding authors upon reasonable request.

**References**

1.      Nitta, N.; Wu, F. X.; Lee, J. T.; Yushin, G. *Mater. Today* **2015,** 18, (5), 252-264.

2.      Tian, C. X.; Lin, F.; Doeff, M. M. *Accounts Chem. Res.* **2018,** 51, (1), 89-96.

3.      Ryu, H. H.; Park, K. J.; Yoon, C. S.; Sun, Y. K. *Chem. Mater.* **2018,** 30, (3), 1155-1163.

4.      Li, L. Z.; Yu, J. G.; Darbar, D.; Self, E. C.; Wang, D. H.; Nanda, J.; Bhattacharya, I.; Wang, C. M. *Acs Energy Lett.* **2019,** 4, (10), 2540-2546.

5.      Zheng, J. M.; Xu, P. H.; Gu, M.; Xiao, J.; Browning, N. D.; Yan, P. F.; Wang, C. M.; Zhang, J. G. *Chem. Mater.* **2015,** 27, (4), 1381-1390.

6.      Armstrong, A. R.; Holzapfel, M.; Novak, P.; Johnson, C. S.; Kang, S. H.; Thackeray, M. M.; Bruce, P. G. *J. Am. Chem. Soc.* **2006,** 128, (26), 8694-8698.

7.      Xu, B.; Fell, C. R.; Chi, M. F.; Meng, Y. S. *Energ. Environ. Sci.* **2011,** 4, (6), 2223-2233.

8.      Gu, M.; Belharouak, I.; Zheng, J. M.; Wu, H. M.; Xiao, J.; Genc, A.; Amine, K.; Thevuthasan, S.; Baer, D. R.; Zhang, J. G.; Browning, N. D.; Liu, J.; Wang, C. M. *Acs Nano* **2013,** 7, (1), 760-767.

9.      Li, L. Z.; Self, E.; Darbar, D.; Zou, L. F.; Bhattacharya, I.; Wang, D. H.; Nanda, J.; Wang, C. M. *Nano Lett.* **2020,** 20, (4), 2756-2762.

10.     Urban, A.; Abdellahi, A.; Dacek, S.; Artrith, N.; Ceder, G. *Physical Review Letters* **2017,** 119, (17), 176402.

11.     Clement, R. J.; Lun, Z.; Ceder, G. *Energ. Environ. Sci.* **2020,** 13, (2), 345-373.

12.     Lee, W.; Muhammad, S.; Sergey, C.; Lee, H.; Yoon, J.; Kang, Y. M.; Yoon, W. S. *Angew. Chem. Int.* **2020,** 59, (7), 2578-2605.

13.     Lee, G. H.; Wu, J. P.; Kim, D.; Cho, K.; Cho, M.; Yang, W. L.; Kang, Y. M. *Angew. Chem. Int.* **2020,** 59, (22), 8681-8688.

14.     Olivetti, E. A.; Ceder, G.; Gaustad, G. G.; Fu, X. K. *Joule* **2017,** 1, (2), 229-243.

15.    Lee, J.; Urban, A.; Li, X.; Su, D.; Hautier, G.; Ceder, G. *Science* **2014,** 343, (6170), 519-522.

16.    Urban, A.; Lee, J.; Ceder, G. *Adv. Energy Mater.* **2014,** 4, (13), 1400478.

17.    Ji, H. W.; Urban, A.; Kitchaev, D. A.; Kwon, D. H.; Artrith, N.; Ophus, C.; Huang, W. X.; Cai, Z. J.; Shi, T.; Kim, J. C.; Kim, H.; Ceder, G. *Nat. Commun.* **2019,** 10, 592.

18.    Freire, M.; Kosova, N. V.; Jordy, C.; Chateigner, D.; Lebedev, O. I.; Maignan, A.; Pralong, V. *Nat. Mater.* **2016,** 15, (2), 173-177.

19.    Yabuuchi, N.; Nakayama, M.; Takeuchi, M.; Komaba, S.; Hashimoto, Y.; Mukai, T.; Shiiba, H.; Sato, K.; Kobayashi, Y.; Nakao, A.; Yonemura, M.; Yamanaka, K.; Mitsuhara, K.; Ohta, T. *Nat. Commun.* **2016,** 7, 13814.

20.    Lee, J. Y.; Papp, J. K.; Clement, R. J.; Sallis, S.; Kwon, D. H.; Shi, T.; Yang, W. L.; McCloskey, B. D.; Ceder, G. *Nat. Commun.* **2017,** 8, 981.

21.    Lun, Z. Y.; Ouyang, B.; Kitchaev, D. A.; Clement, R. J.; Papp, J. K.; Balasubramanian, M.; Tian, Y. S.; Lei, T.; Shi, T.; McCloskey, B. D.; Lee, J.; Ceder, G. *Adv. Energy Mater.* **2019,** 9, (2), 1802959.

22.    Jones, M. A.; Reeves, P. J.; Seymour, I. D.; Cliffe, M. J.; Dutton, S. E.; Grey, C. P. *Chemical Communications* **2019,** 55, (61), 9027-9030.

23.    Cambaz, M. A.; Urban, A.; Pervez, S. A.; Gesswein, H.; Schiele, A.; Guda, A. A.; Bugaev, A. L.; Mazilkin, A.; Diemant, T.; Behm, R. J.; Brezesinski, T.; Fichtner, M. *Chem. Mater.* **2020,** 32, (8), 3447-3461.

24.    Cambaz, M. A.; Vinayan, B. P.; Euchner, H.; Pervez, S. A.; Gesswein, H.; Braun, T.; Gross, A.; Fichtner, M. *Acs Appl. Mater. Inter.* **2019,** 11, (43), 39848-39858.

25.    Nakajima, M.; Yabuuchi, N. *Chem. Mater.* **2017,** 29, (16), 6927-6935.

26.    Kitchaev, D. A.; Lun, Z. Y.; Richards, W. D.; Ji, H. W.; Clement, R. J.; Balasubramanian, M.; Kwon, D. H.; Dai, K. H.; Papp, J. K.; Lei, T.; McCloskey, B. D.; Yang, W. L.; Lee, J.; Ceder, G. *Energ. Environ. Sci.* **2018,** 11, (8), 2159-2171.

27.    Seo, D. H.; Lee, J.; Urban, A.; Malik, R.; Kang, S.; Ceder, G. *Nat. Chem.* **2016,** 8, (7), 692-697.

28.    Yabuuchi, N.; Takeuchi, M.; Nakayama, M.; Shiiba, H.; Ogawa, M.; Nakayama, K.; Ohta, T.; Endo, D.; Ozaki, T.; Inamasu, T.; Sato, K.; Komaba, S. *Proceedings of the National Academy of Sciences of the United States of America* **2015,** 112, (25), 7650-7655.

29.    Richards, W. D.; Dacek, S. T.; Kitchaev, D. A.; Ceder, G. *Adv. Energy Mater.* **2018,** 8, (5), 1701533.

30.    Lee, J.; Kitchaev, D. A.; Kwon, D. H.; Lee, C. W.; Papp, J. K.; Liu, Y. S.; Lun, Z. Y.; Clement, R. J.; Shi, T.; McCloskey, B. D.; Guo, J. H.; Balasubramanian, M.; Ceder, G. *Nature* **2018,** 556, (7700), 185.

31.    Ouyang, B.; Artrith, N.; Lun, Z. Y.; Jadidi, Z.; Kitchaev, D. A.; Ji, H. W.; Urban, A.; Ceder, G. *Adv. Energy Mater.* **2020,** 10, (10), 1903240.

32.    Chen, R. Y.; Ren, S. H.; Knapp, M.; Wang, D.; Witter, R.; Fichtner, M.; Hahn, H. *Adv. Energy Mater.* **2015,** 5, (9), 1401814.

33.    Takeda, N.; Hoshino, S.; Xie, L.; Chen, S.; Ikeuchi, I.; Natsui, R.; Nakura, K.; Yabuuchi, N. *J. Power Sources* **2017,** 367, 122-129.

34.    Wang, Z. L.; Yin, J. S.; Jiang, Y. D. *Micron* **2000,** 31, (5), 571-580.

35.    Guo, H. Z.; Li, Q. Q.; Yang, Z. Z.; Jin, K. J.; Ge, C.; Gu, L.; He, X.; Li, X. L.; Zhao, R. Q.; Wan, Q.; Wang, J. S.; He, M.; Wang, C.; Lu, H. B.; Yang, Y. P.; Yang, G. Z. *Scientific Reports* **2017,** 7, 7693.

36.    Xia, K. Y.; Nan, P. F.; Tan, S. H.; Wang, Y. M.; Ge, B. H.; Zhang, W. Q.; Anand, S.; Zhao, X. B.; Snyder, G. J.; Zhu, T. J. *Energ. Environ. Sci.* **2019,** 12, (5), 1568-1574.

37.    Kwon, D.-H.; Lee, J.; Artrith, N.; Kim, H.; Wu, L.; Lun, Z.; Tian, Y.; Zhu, Y.; Ceder, G. *Cell Reports Physical Science* **2020,** 1, (9), 100187.

38.    Pennycook, S. J. *Springer* **2011**, New York, NY.

39.    Van der Ven, A.; Deng, Z.; Banerjee, S.; Ong, S. P. *Chemical Reviews* **2020,** 120, (14), 6977-7019.

40.    Ahn, J.; Chen, D. C.; Chen, G. Y. *Adv. Energy Mater.* **2020,** 10, 2001671.

41.    Yue, Y.; Li, N.; Li, L. Z.; Foley, E. E.; Fu, Y. B.; Battaglia, V. S.; Clement, R. J.; Wang, C. M.; Tong, W. *Chem. Mater.* **2020,** 32, (11), 4490-4498.

42.    Crafton, M. J.; Yue, Y.; Huang, T. Y.; Tong, W.; McCloskey, B. D. *Adv. Energy Mater.* **2020,** 10, 2001500.

43.    Yan, P. F.; Zheng, J. M.; Tang, Z. K.; Devaraj, A.; Chen, G. Y.; Amine, K.; Zhang, J. G.; Liu, L. M.; Wang, C. M. *Nature Nanotechnology* **2019,** 14, (6), 602-608.

44.    Xiao, P. H.; Deng, Z. Q.; Manthiram, A.; Henkelman, G. *J. Phys. Chem. C* **2012,** 116, (44), 23201-23204.

45.    Shin, Y.; Kan, W. H.; Aykol, M.; Papp, J. K.; McCloskey, B. D.; Chen, G. Y.; Persson, K. A. *Nat. Commun.* **2018,** 9, 4597.

46.    Armstrong, A. R.; Bruce, P. G. *Nature* **1996,** 381, (6582), 499-500.

47.    Capitaine, F.; Gravereau, P.; Delmas, C. *Solid State Ionics* **1996,** 89, (3-4), 197-202.

48.     Ammundsen, B.; Desilvestro, J.; Groutso, T.; Hassell, D.; Metson, J. B.; Regan, E.; Steiner, R.; Pickering, P. J. *J. Electrochem. Soc.* **2000,** 147, (11), 4078-4082.

49.     Ammundsen, B.; Paulsen, J. *Adv. Mater.* **2001,** 13, (12-13), 943.

50.     Reed, J.; Ceder, G.; Van der Ven, A. *Electrochem. Solid-State Lett.* **2001,** 4, (6), A78-A81.

51.     Leifer, N.; Schipper, F.; Erickson, E. M.; Chanty, C.; Talianker, M.; Grinblat, J.; Julien, C. M.; Markovsky, B.; Aurbach, D. *J. Phys. Chem. C* **2017,** 121, (17), 9120-9130.

52.     Reed, J.; Ceder, G. *Chemical Reviews* **2004,** 104, (10), 4513-4533.

53.     Xu, C.; Reeves, P. J.; Jacquet, Q.; Grey, C. P. *Advanced Energy Materials* **2020,** 11, 2003404.

54.     Ji, H. W.; Wu, J. P.; Cai, Z. J.; Liu, J.; Kwon, D. H.; Kim, H.; Urban, A.; Papp, J. K.; Foley, E.; Tian, Y. S.; Balasubramanian, M.; Kim, H.; Clement, R. J.; McCloskey, B. D.; Yang, W. L.; Ceder, G. *Nat. Energy* **2020,** 5, (3), 213-221.

**Author Contributions:**

L.L. carried out the STEM analysis, Z.L., D.C., Y.Y., W.T., and G.C. synthesized the samples and carried out the electrochemical testing, G.C. and C.W. supervised the research. L.L. and Z.L. analyzed the data and drafted the manuscript with final approval by all authors.

**Competing financial interests**:

The authors declare no competing financial interest.

**Additional Information**:
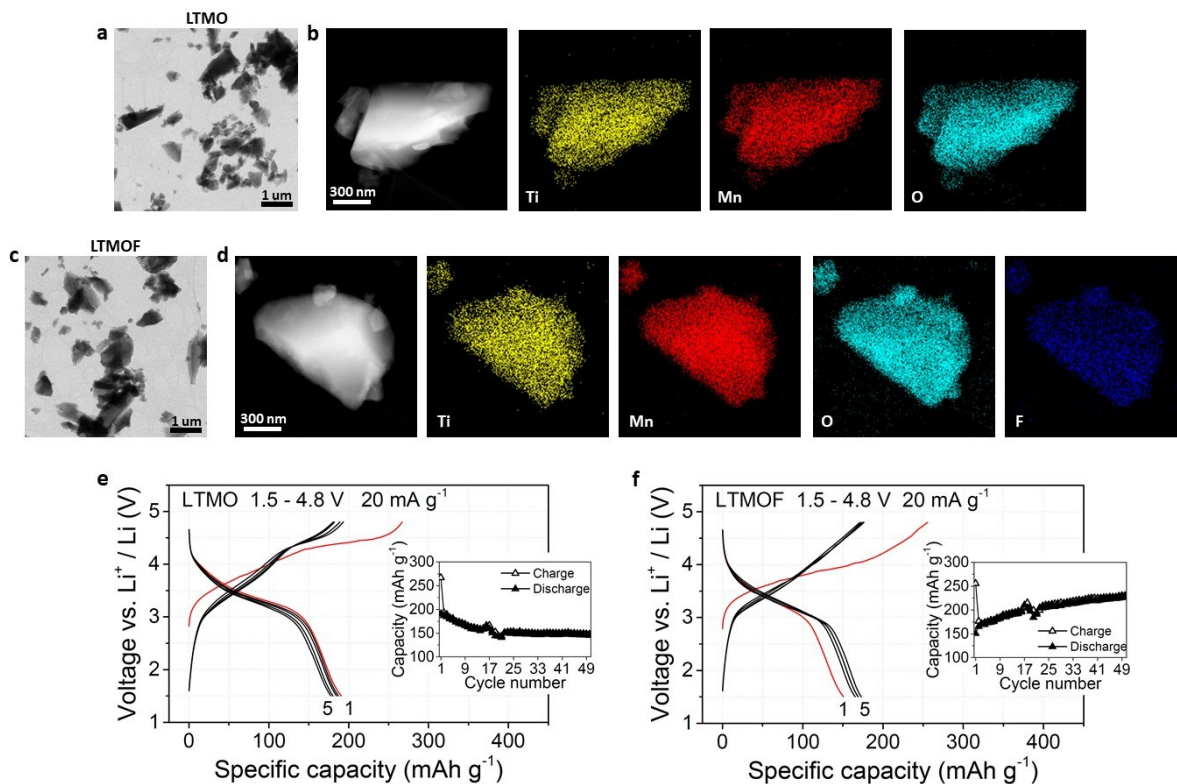
Supplementary Figure S1-S17, Table S1-S3.

**Figure 1 | Morphology, composition, and electrochemical properties of LTMO and LTMOF particles.** (a) TEM image of pristine LTMO particles. (b) STEM image and corresponding EDS elemental maps of a pristine LTMO particle. (c) TEM image of pristine LTMOF particles. (d) STEM image and corresponding EDS elemental maps of a pristine LTMOF particle. (e,f) Charge and discharge voltage profiles for the 1st, 10th, 25th, and 50th cycles and specific capacity as a function of cycle number (inset) for LTMO (e) and LTMOF (f) cathodes in half-cells cycled between 1.5 and 4.8 V at a current density of 20 mA g$^{-1}$. The capacity fluctuation near the 18th cycle in both tests was caused by unintended temperature fluctuation.
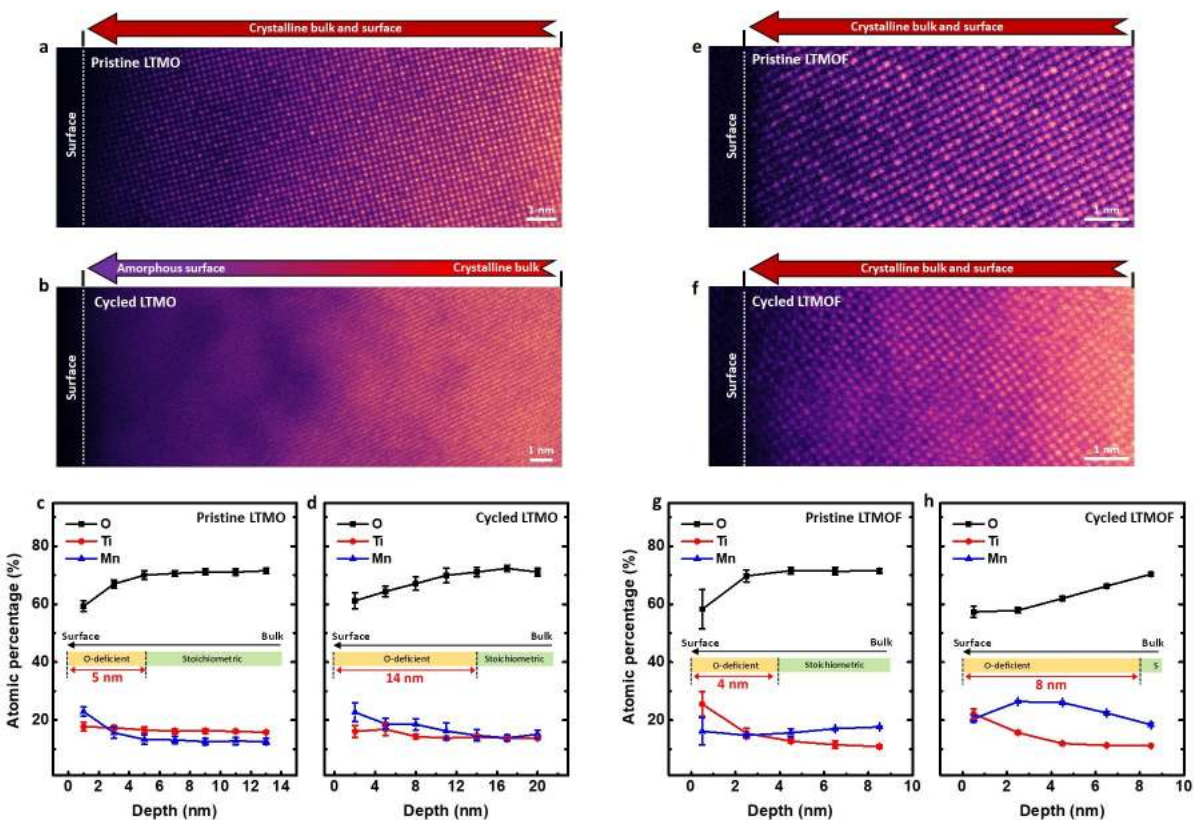
15

**Figure 2 | Structural and chemical evolution in LTMO and LTMOF cathodes induced by cycling.** (a,b) Atomic-resolution STEM HAADF images of nanoscale surface regions in LTMO in the pristine state (a) and in the discharged state after 50 cycles (b). (c,d) Extracted atomic-percentage profiles of Ti, Mn, and O within nanoscale regions below the surface of pristine (c) and cycled (d) LTMO particles based on EELS measurements. The EELS spectra were collected at 7 different locations below the surface (see supporting information). (e,f) Atomic-resolution STEM HAADF images of nanoscale surface regions in LTMOF in the pristine state (e) and in the discharged state after 50 cycles (f). (g,h) Extracted atomic-percentage profiles of Ti, Mn, and O within nanoscale regions below the surface of pristine (g) and cycled (h) LTMOF particles based on EELS measurements. The EELS spectra were collected at 5 different locations below the surface (see supporting information). Note that due to the low concentration of F in LTMOF, the F *K*-edges cannot be detected by EELS in our work and thus only Ti, Mn, and O are quantified here. Therefore, the sum of the atomic percentages of Ti, Mn, and O equals 100% at each point in (c,d) and (g,h).
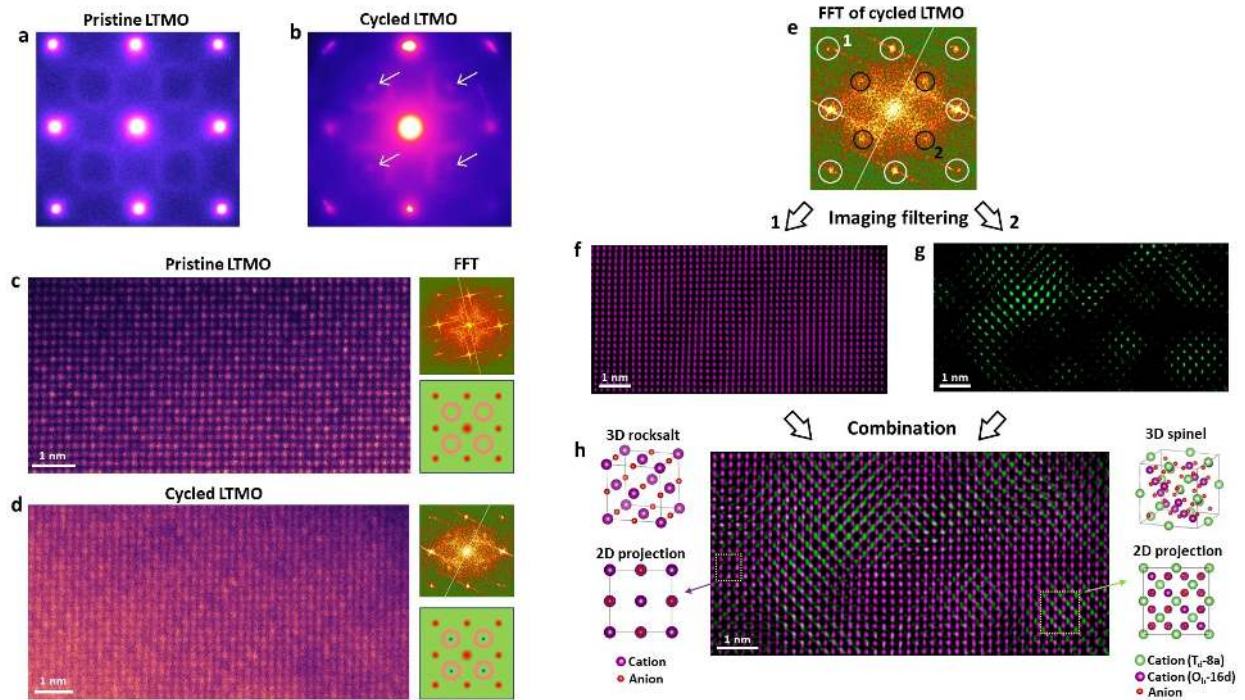
**Figure 3 | Structural transformation in LTMO cathode induced by cycling.** (a,b) Electron diffraction patterns for pristine LTMO (a) and discharged LTMO after 50 cycles (b). The white arrows in (b) mark the 4 additional spots corresponding to the spinel-like lattice. (c) Atomic-resolution STEM HAADF image of a nanoscale bulk region in pristine LTMO (left), corresponding fast Fourier transform (FFT) (top right), and schematic for the Fourier transform (bottom right). (d) Atomic-resolution STEM HAADF image of a nanoscale bulk region in discharged LTMO after 50 cycles (left), corresponding Fourier transform (top right), and schematic for the Fourier transform (bottom right). (e-f) Procedures and results of STEM HAADF image filtering. In the FFT (e), white-colored filtering masks that only allow structural information from the rocksalt cubic lattice were applied, and an inverse Fourier transform was performed, resulting in a filtered image (f) that only contains rocksalt structures. Black-colored filtering masks that only allow structural information from the spinel-like lattice were applied, and an inverse Fourier transform was performed, resulting in a filtered image (g) that only contains spinel-like structures. A combination of (f) and (g) results in a single filtered image (h) showing the spatial distribution of rocksalt (purple) and spinel-like (green) structures. 3D and 2D atomic models of rocksalt and spinel structures are shown on the left and right sides of the filtered image, respectively.
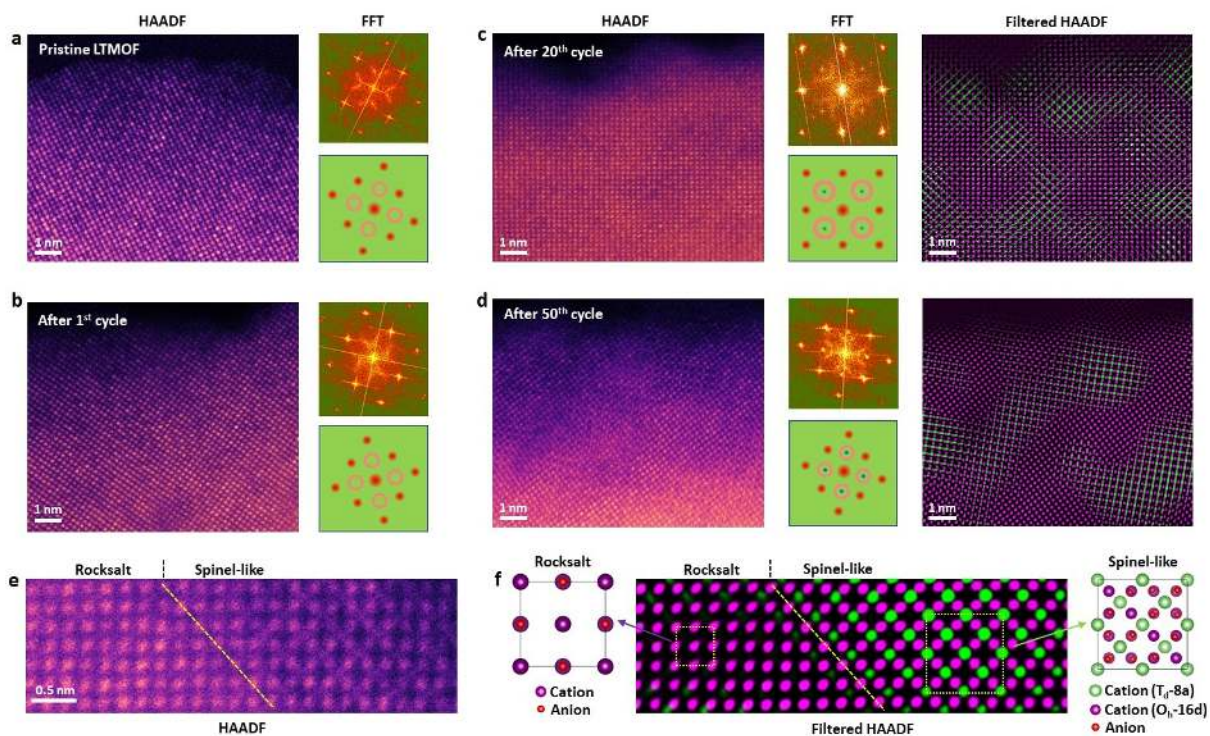
**Figure 4 | Structural transformation in LTMOF cathode induced by cycling.** (a) Atomic-resolution STEM HAADF image of a nanoscale region in pristine LTMOF (left), corresponding fast Fourier transform (FFT) (top right), and schematic for the Fourier transform (bottom right). (b) Atomic-resolution STEM HAADF image of a nanoscale region in discharged LTMOF after the 1st cycle (left), corresponding Fourier transform (top right), and schematic for the Fourier transform (bottom right). (c) Atomic-resolution STEM HAADF image of a nanoscale region in discharged LTMOF after 20 cycles (left), corresponding Fourier transform (top middle), schematic for the Fourier transform (bottom middle), and corresponding filtered STEM HAADF image (right) showing the spatial distribution of rocksalt (purple) and spinel-like (green) structures. (d) Atomic-resolution STEM HAADF image of a nanoscale region in discharged LTMOF after 50 cycles (left), corresponding Fourier transform (top middle), schematic for the Fourier transform (bottom middle), and corresponding filtered STEM HAADF image (right) showing the spatial distribution of rocksalt (purple) and spinel-like (green) structures. (e) Magnified STEM HAADF image of a boundary across rocksalt and spinel-like structures in cycled LTMOF. (f) Corresponding filtered image of the magnified STEM HAADF image in (e), showing the spatial distribution of rocksalt (purple) and spinel-like (green) structures. 2D atomic models of rocksalt and spinel structures are shown on the left and right sides of the filtered image, respectively.
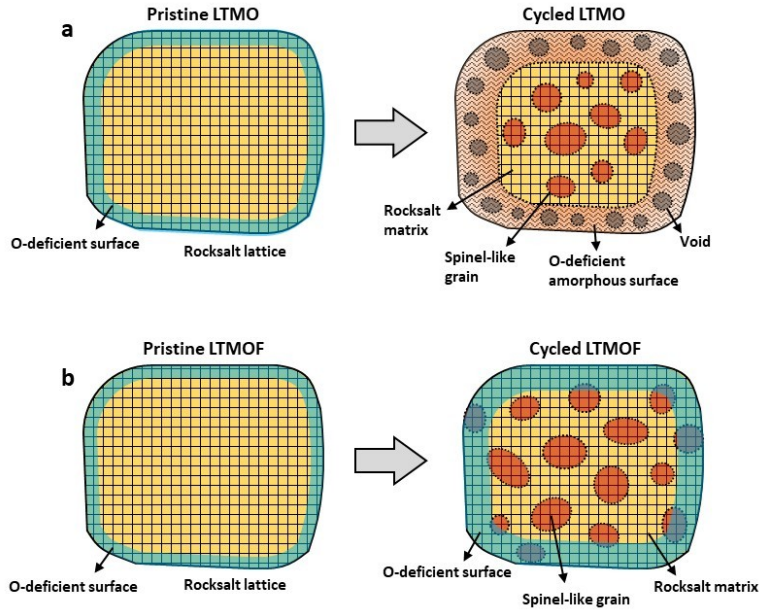
18

**Figure 5 | Schematic illustration of structural and chemical evolution in LTMO and LTMOF induced by cycling.** (a) In LTMO, electrochemical cycling results in surface degradation, such as amorphization and void formation, and rocksalt-to-spinel-like structural transformation within nanosized grains dispersed in the DRX matrix. (b) In LTMOF, electrochemical cycling results in rocksalt-to-spinel-like structural transformation within nanosized grains dispersed in the DRX matrix, whereas the crystalline surface remains well preserved.